PHYSICAL REVIEW B **109**, 205141 (2024)

Comprehensive study of all spinful and spinless linear band crossings in the 80 layer groups

Wencheng Wang,[1,2] Liangliang Huang,[1] Xiangang Wan,[1,3] and Feng Tang[1,*]
[1]*National Laboratory of Solid State Microstructures and School of Physics, Nanjing University, Nanjing 210093, China*
and Collaborative Innovation Center of Advanced Microstructures, Nanjing University, Nanjing 210093, China
[2]*International Quantum Academy, Shenzhen 518048, China*
[3]*Hefei National Laboratory, Hefei 230088, China*

(Received 28 December 2023; revised 10 April 2024; accepted 29 April 2024; published 20 May 2024)

Two-dimensional (2D) materials have emerged as a fertile ground displaying various fascinating properties, such as nontrivial band topology and exotic correlated states, which can be feasibly tuned by available means (e.g., electrostatic gating, stacking, sliding, and twist). Due to the scarcity of ever-experimentally synthesized 2D materials, large-scale target searches on 2D materials have been hindered. Here we focus our attention on all linear band crossings (LBCs) at high-symmetry points, lines, and planes that can be realized in the 80 layer groups (LGs) with (without) time-reversal symmetry using single-valued and double-valued representations (corresponding to spinless and spinful bands, respectively), and list all corresponding $k \cdot p$ models expanded up to the first order of $\vec{q} = (q_x, q_y)$ (measured from the LBC). The relations of symmetry-related LBCs are explicitly provided, useful in studies on valley degrees of freedom, which have been overlooked in previous classifications on band crossings by space and layer groups to our knowledge. The results of 17 LGs, as wallpaper groups, can be applied to surfaces and interfaces of 3D materials or 2D materials grown on substrates. By exhaustive tabulation on all LBCs in the 80 LGs, we highlight LGs hosting LBCs that are enforced to exist necessarily. These LGs are then applied to categorize the 6351 2D structures in the 2D materials database (2DMatPedia) to 1707 (3035) materials necessarily hosting coexisting spinful and spinless LBCs (only necessarily hosting spinful LBCs). We also perform first-principles calculations on 66 selected 2D materials to identify the LBCs at high-symmetry points quantitatively in electronic and phononic bands. We take Zr_2HBr_2 crystallized in LG 15 to demonstrate the coexisting electronic Dirac nodal point and phononic Weyl nodal line emanating from a Weyl LBC. The group-theoretical results are expected to guide searches and designs for materials realization for a target LBC in 2D materials, coexisting LBCs carried by different types of excitations, and can also be applied to study the evolution of topological band crossings by external perturbations in the future.

DOI: 10.1103/PhysRevB.109.205141

I. INTRODUCTION

The low-energy excitations around the corners of the Brillouin zone (BZ) in the first-synthesized two-dimensional (2D) material (graphene) simulate high-energy massless Dirac fermions in two dimensions [1], underlying a zoo of unique properties [2], such as ultrahigh mobility [1], Klein tunneling [3,4], half-integer quantum Hall effect [5,6], quantum anomalous Hall effect [7–11], quantum spin Hall effect [12–16], valley Hall effect [17–19], nonlinear Hall effect [20–22], topological band crossings [23–26], and so on. In the past two decades, more than 100 2D materials have been synthesized with diverse chemical compositions and structure symmetries [1,27–39], as well as several computationally predicted 2D materials databases [40–46], providing a fruitful platform for studying properties that can be manipulated by stacking [47], twisting [48–50], electrostatic gating [51,52], and other appropriate means to control and optimize physical properties.

On the other hand, symmetry analysis can provide a general guidance of studying materials properties. For example, a general theory of ferroelectricity based on the 80 layer groups (LGs) was built very recently [53], guiding researchers to alter the electric polarization by sliding and twisting two adjacent 2D materials. Compared with 2D materials, the 3D materials can accommodate much more fruitful band crossings [54–67]. The space groups for three-dimensional (3D) crystals have been applied to obtain a complete classification of band topology [68–73] and database searches [74–79]. Very recently, several groups have also constructed exhaustive tabulations of all band crossings in the 230 space groups (SGs), 1651 magnetic space groups [80–84], and the 80 layer groups and 528 magnetic layer groups for 2D crystals [82,85,86]. These exhaustive results conclude all possible stable degeneracies (2, 3, 4, 6, and 8) realized in band structures [80,82]. Charting the band crossings in these works based on the magnetic space and layer groups facilitate users to search for and design materials given a target band crossing: First, know which magnetic space and layer group(s) could realize it, then search for materials crystallized in any of these magnetic space and layer group(s), and, lastly, determine the detailed information (e.g., position in the BZ and energetics) of the target band crossing by realistic calculations. Interestingly, some band crossings can be enforced to appear necessarily insofar as

---

[*] fengtang@nju.edu.cn

the material belongs to the required magnetic space (layer) group, in which case, the target band crossing's existence is guaranteed. Moreover, external perturbations preserving the crystallographic symmetry can be imposed to optimize the band structures toward realization of an ideal band crossing, which necessarily exists in the whole optimization process.

In this paper, we focus on the 80 LGs applicable for 2D materials, and band crossings with linear dispersion [dubbed linear band crossing (LBC) hereafter]: The $k \cdot p$ models around the LBCs are expanded up to the first order in $\vec{q} = (q_x, q_y)$ (measured from the LBC). We note that the order in the $\vec{q}$ of $k \cdot p$ model and the dispersion near a band crossing have received immense attention while limiting only to the first order reasonably avoids the trivial $q^2(= q_x^2 + q_y^2)$ term that can always be allowed to exist and break the emergent chiral symmetry. Note that several LBCs can be related by LG operations, so only one representative LBC among the symmetry-related LBCs need to be studied. However, explicitly listing all symmetry-related LBCs could be useful in analyzing valley-related properties. Here, we tabulate all symmetry-related LBCs and how the representation matrices and their $k \cdot p$ models are related explicitly. In total, we construct 2183 LBCs by considering all high-symmetry points (HSPs), high-symmetry lines (HSLs), and high-symmetry planes (HSPLs). During the construction, both the spinful and spinless settings are considered and time-reversal symmetry (TRS) can be broken or present. The single-valued and double-valued representations are applied for the spinless and spinful settings, respectively. The spinful and spinless settings can be applied to electronic bands with negligible and non-negligible spin-orbit coupling (SOC), respectively: For electronic bands, when the SOC can be neglected, the degeneracy we list in the spinless setting should be doubled to derive a genuine degeneracy. The results in the spinless setting can also be applied to bosonic systems, such as phonon [87,88], photon [89], and magnon [90] systems. In the following, we use the abbreviations NSOC and SOC to indicate the spinless and spinful settings, respectively.

We provide all positions of LBCs and all explicit representation matrices for the little groups of the LBCs as well as all symmetry-related LBCs in Supplemental Material (SM) I [91]. The statistics of numbers of LBCs is given in Table I for LBCs that can emerge in 2D materials in the four settings denoted by NTRS, NSOC; NTRS, SOC; TRS, NSOC; and TRS, SOC [TRS (NTRS): TRS is present (broken)]. By the exhaustive tabulation, some generic and unified conclusions can be deduced. For example, the degeneracy of LBC can only be 2 or 4 with the corresponding LBC denoted as a Weyl or Dirac LBC, respectively. The total number of symmetry-related LBCs (with the same energies) for the Weyl LBC can be 1, 2, 3, 4, 6, 8, 12 for the NTRS, NSOC and NTRS, SOC settings; 1, 2, 4, 6, 8, 12 for the TRS, NSOC setting; and 1, 2, 3, 4, 6, 12 for the TRS, SOC setting. Differently, the Dirac LBC cannot appear in the NTRS, NSOC setting. The Dirac LBC can only appear at one single HSP in the NTRS, SOC setting. In both TRS, NSOC and TRS, SOC settings, the total number of symmetry-related Dirac LBCs can be 1, 2, 4. We'll provide detailed discussions on all possible $k \cdot p$ models and the nodal structures and chiral symmetries by $k \cdot p$ models in the following.

In addition, results obtained purely from the 80 LGs could provide not only unified pictures of seemingly diverse phenomena but also hints for reliable and efficient materials prediction. We highlight the LGs for which there exists an LBC which necessarily appears at some k point in some setting. These LGs can be applied to quickly identify concrete 2D materials with LBCs without any realistic calculations. For electronic band structures, the ideal LBC should be close to the Fermi level, which can be satisfied more easily in that LBCs necessarily appear. Note that when SOC is negligibly weak, the LBC proposed in the spinless setting can coexist in the electronic bands and phononic bands. However, LBC might be gapped by finite SOC in electronic bands, and whether LBCs can coexist in the electronic bands (with non-negligible SOC) and phononic bands deserves careful study. Hereafter, SOC is always included for electronic bands. We then find 37 or 30 LGs, with necessarily coexisting spinful and spinless LBCs when TRS is preserved or broken, respectively. We then perform a large-scale classification on the 6351 2D materials as listed in 2DMatPedia and tabulate 1707 (3035) materials necessarily hosting coexisting electronic and phononic LBCs (only necessarily hosting electronic LBC) listed in SM II [92]. In SM II [92], we also show the first-principles calculated electronic and phononic bands of 66 selected 2D materials, with all LBCs pinned at HSPs identified.

This paper is organized as follows. In Sec. II, we briefly describe the method of obtaining all LBCs in the 80 LGs and the organization of SM I consisting of a full tabulation of all LBCs. The nodal structures and possible chiral symmetries determined by the constructed $k \cdot p$ models are also described. Then, in Sec. III, LGs necessarily hosting LBCs are listed

TABLE I. Statistics of LBCs in the 80 LGs. The four settings are denoted by NTRS, NSOC; NTRS, SOC; TRS, NSOC; and TRS, SOC in the first column, corresponding to the settings without TRS and neglecting SOC, without TRS and considering SOC, with TRS and neglecting SOC, with TRS and considering SOC, respectively. We consider symmetry-independent k points and LBCs in the statistics. We show the numbers of k points and LBCs outside and inside the parentheses, respectively. Note that the setting neglecting SOC can be applied to bosonic systems.

Setting	HSP	HSL	HSPL
NTRS, NSOC	70 (98)	200 (510)	37 (37)
NTRS, SOC	116 (152)	200 (280)	37 (37)
TRS, NSOC	78 (111)	202 (498)	37 (37)
TRS, SOC	198 (248)	136 (160)	15 (15)

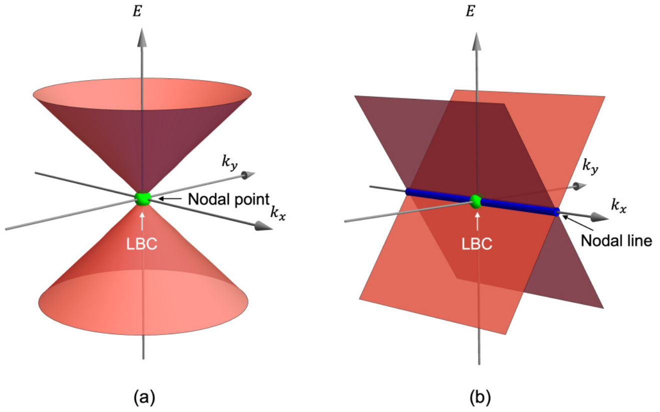

FIG. 1. Schematic diagram of LBC and two types of nodal structures: Nodal point and nodal line are shown in (a) and (b), respectively. Green sphere indicates the LBC; one point in the BZ where two branches of bands touch. The blue line in (b) indicates a nodal line emanating from the LBC which preserves the degeneracy of the LBC.

in detail, where LGs with necessarily coexisting spinful and spinless LBC are highlighted. Sections IV and V are devoted to the demonstration of applying our tabulation to quickly identity all LBCs given an LG and large-scale materials investigation by a 2D materials database, respectively. Finally, the calculation method and conclusion (and discussion) are provided in Secs. VI and VII, respectively.

II. ALL WEYL AND DIRAC LBCS CLASSIFIED BY THE 80 LGS

A. Tabulation of all LBCs in the 80 LGs

An LBC is defined as one point in the BZ, where two branches of bands touch, as schematically shown in Fig. 1. By exhausting all 80 LGs, considering the four settings, NTRS, NSOC; NTRS, SOC; TRS, NSOC; and TRS, SOC (without TRS and neglecting SOC, without TRS and considering SOC, with TRS and neglecting SOC, with TRS and considering SOC, respectively), we find that the LBCs can only be two- or fourfold degenerate (denoted as Weyl LBCs or Dirac LBCs, respectively). These LBCs are restricted to be located at the HSP, HSL, or HSPL. Note that the HSPL coincides with the 2D BZ. An LBC at the HSP contains only one irreducible representation (irrep) or irreducible corepresentation (coirrep) [93] of dimension 2 or 4, an LBC in the HSL might contain one or two different (co)irreps, while an LBC in the HSPL contains two different (co)irreps [82]. Note that the HSPL can only host one-dimensional (coirrep, so the LBC in the HSPL is definitely twofold degenerate. In addition, each HSPL hosts one LBC at most, as shown in Table I. Note that the coirrep for a little group of any k point is applied to characterize each energy level at the k point (assuming no accidental degeneracy), if and only if the little group contains an antiunitary operation in the form of ΘR, where Θ denotes the time-reversal operation and R represents a spatial operation in the LG. We fix the convention for the 80 LGs so the c axis is perpendicular to the 2D material, and all LG operations can be found in Ref. [94] (note that the operations are also listed in SM I [91]). We also show all the Cartesian coordinates for the conventional lattice basis vectors $\vec{a}, \vec{b}, \vec{c}$ and the transformation matrix A_{cp} from the conventional lattice basis vectors to the primitive lattice basis vectors $\vec{a}_1, \vec{a}_2, \vec{a}_3$ in SM I [91]. The lattice of LG can only be primitive or centered and, correspondingly, $\vec{a}_1 = \vec{a}, \vec{a}_2 = \vec{b}, \vec{a}_3 = \vec{c}$ $\left(A_{cp} = \begin{pmatrix} 1 & 0 & 0 \\ 0 & 1 & 0 \\ 0 & 0 & 1 \end{pmatrix}\right)$ or $\vec{a}_1 = \frac{1}{2}\vec{a} + \frac{1}{2}\vec{b}, \vec{a}_2 = -\frac{1}{2}\vec{a} + \frac{1}{2}\vec{b}, \vec{a}_3 = \vec{c}$ $\left(A_{cp} = \begin{pmatrix} \frac{1}{2} & -\frac{1}{2} & 0 \\ \frac{1}{2} & \frac{1}{2} & 0 \\ 0 & 0 & 1 \end{pmatrix}\right)$, respectively.

In total, we collect 2183 LBCs (only independent ones are counted) including 2091 Weyl and 92 Dirac LBCs, and there are in total 4953 LBCs counting all symmetry-related LBCs. Note that one LBC is characterized by its location and the contained (co)irrep(s). In Table II, we list the LGs allowing the occurrence of Weyl (Dirac) LBC for each of the four settings. For example, the Weyl LBC can appear in LG 80 for the TRS, NSOC setting, as exemplified by graphene. The Dirac LBC in the spinful setting with TRS can appear in 30 LGs (LGs 7, 15–17, 21, 25, 28–30, 32–34, 38–46, 48, 52, 54, 56, 58, 60, 62–64), as proposed in Ref. [24] and tabulated in Ref. [95]. The Dirac LBC in the spinless setting with TRS can appear in seven LGs (LGs 29, 33, 40, 43-45, 63), as discussed for Dirac phonons in Ref. [96]. For these LBCs, we construct the $k \cdot p$ models up to the first order of $\vec{q}$. Interestingly, we find that there are 165 different $k \cdot p$ models in total, listed in Table SI2 of SM I: $H_i, i = 1, 2, \dots, 115$ are 2×2 while the rest are 4×4, enough to describe all LBCs in the 80 LGs. These $k \cdot p$ models are then expected to be reasonable starting points to study low-energy behaviors adding interactions, disorder and external fields to exhaust the possible outcomes for 2D systems. We list for the four settings the possible $k \cdot p$ models for Weyl (Dirac) LBCs in Table III. Note that other than these 4953 LBCs which can be identified by computing representations of energy bands, there exists a twofold degenerate LBC that can be located at a generic point (GP) whose identification needs computing Berry phase. Such kind of LBC might occur when $C_{2z}\Theta$ (C_{2z}: twofold rotation around z axis) is present in either a spinless or spinful setting, or when $I\Theta$ (I: spatial

TABLE II. The list of LGs which host twofold degenerate Weyl LBCs and fourfold degenerate Dirac LBCs.

Setting	LGs hosting Weyl LBCs	LGs hosting Dirac LBCs
NTRS, NSOC	4–48, 51–64, 67–72, 74–80	
NTRS, SOC	4–48, 51–64, 67–72, 74–80	62, 64
TRS, NSOC	4–48, 51–64, 66–80	29, 33, 40, 43, 44, 45, 63
TRS, SOC	1, 3–5, 8–13, 19–36, 49, 50, 53–60, 65, 67–70 73, 74, 76–79	7, 15–17, 21, 25, 28–30, 32–34, 38–46, 48, 52, 54, 56, 58 60, 62–64

TABLE III. The list of all possible $k \cdot p$ models of twofold degenerate Weyl LBCs and fourfold degenerate Dirac LBCs in the 80 LGs in the four settings. The $k \cdot p$ models are given by H_i, $i = 1, 2, 3, \ldots, 165$, whose explicit form can be found in Table SI2 of SM I.

Setting	$k \cdot p$ models of Weyl LBCs	$k \cdot p$ models of Dirac LBCs
NTRS, NSOC	$H_3, H_5, H_8, H_{10}, H_{16}, H_{23}, H_{24}, H_{25}, H_{29}, H_{30}, H_{34}, H_{39}, H_{40}, H_{45}, H_{48}, H_{49}, H_{50}, H_{51}, H_{54}, H_{55}, H_{57}, H_{61}, H_{62}, H_{64}, H_{65}, H_{66}, H_{67}, H_{68}, H_{71}, H_{78}, H_{79}, H_{83}, H_{87}, H_{88}, H_{89}, H_{91}, H_{101}, H_{103}, H_{104}, H_{105}, H_{107}, H_{113}$	
NTRS, SOC	$H_3, H_5, H_9, H_{10}, H_{16}, H_{23}, H_{24}, H_{25}, H_{29}, H_{30}, H_{31}, H_{34}, H_{35}, H_{39}, H_{40}, H_{44}, H_{46}, H_{48}, H_{49}, H_{50}, H_{51}, H_{52}, H_{54}, H_{55}, H_{57}, H_{61}, H_{62}, H_{63}, H_{65}, H_{68}, H_{69}, H_{70}, H_{75}, H_{78}, H_{79}, H_{80}, H_{81}, H_{84}, H_{87}, H_{88}, H_{89}, H_{91}, H_{92}, H_{93}, H_{94}, H_{95}, H_{97}, H_{98}, H_{99}, H_{100}, H_{102}, H_{105}, H_{107}, H_{109}, H_{110}, H_{111}, H_{112}, H_{114}$	H_{162}, H_{164}
TRS, NSOC	$H_3, H_5, H_6, H_8, H_{10}, H_{12}, H_{13}, H_{16}, H_{18}, H_{19}, H_{21}, H_{22}, H_{25}, H_{26}, H_{27}, H_{28}, H_{29}, H_{30}, H_{32}, H_{33}, H_{36}, H_{37}, H_{40}, H_{41}, H_{47}, H_{48}, H_{49}, H_{50}, H_{51}, H_{53}, H_{54}, H_{56}, H_{60}, H_{61}, H_{62}, H_{66}, H_{68}, H_{71}, H_{72}, H_{73}, H_{74}, H_{76}, H_{77}, H_{78}, H_{79}, H_{82}, H_{83}, H_{85}, H_{86}, H_{88}, H_{89}, H_{90}, H_{96}, H_{101}, H_{107}, H_{108}, H_{113}, H_{115}$	$H_{124}, H_{125}, H_{134}, H_{141}, H_{142}, H_{148}, H_{149}, H_{154}$
TRS, SOC	$H_1, H_2, H_3, H_4, H_5, H_6, H_7, H_{10}, H_{11}, H_{12}, H_{13}, H_{14}, H_{15}, H_{16}, H_{17}, H_{19}, H_{20}, H_{21}, H_{26}, H_{29}, H_{30}, H_{31}, H_{32}, H_{33}, H_{35}, H_{36}, H_{37}, H_{38}, H_{41}, H_{42}, H_{43}, H_{44}, H_{46}, H_{47}, H_{48}, H_{49}, H_{50}, H_{51}, H_{52}, H_{53}, H_{54}, H_{55}, H_{56}, H_{58}, H_{59}, H_{60}, H_{85}, H_{86}, H_{88}, H_{89}, H_{90}, H_{92}, H_{93}, H_{96}, H_{99}, H_{100}, H_{105}, H_{106}, H_{107}, H_{108}, H_{109}, H_{110}, H_{111}, H_{112}, H_{113}, H_{114}$	$H_{116}, H_{117}, H_{118}, H_{119}, H_{120}, H_{121}, H_{122}, H_{123}, H_{124}, H_{125}, H_{126}, H_{127}, H_{128}, H_{129}, H_{130}, H_{131}, H_{132}, H_{133}, H_{135}, H_{136}, H_{137}, H_{138}, H_{139}, H_{140}, H_{143}, H_{144}, H_{145}, H_{146}, H_{147}, H_{150}, H_{151}, H_{152}, H_{153}, H_{155}, H_{156}, H_{157}, H_{158}, H_{159}, H_{160}, H_{161}, H_{163}, H_{165}$

inversion operation) is present in the spinless setting. Here, for the TRS, NSOC/TRS, SOC setting, LGs need to contain C_{2z} and for the TRS, NSOC setting, LGs need to contain I to allow the twofold LBC at the GP. The $k \cdot p$ model around such kind of LBC can be written as $-\frac{1}{2}\sigma_0(r_1 q_x + r_3 q_y) - \frac{1}{\sqrt{2}}\sigma_1(r_5 q_x + r_6 q_y) + \frac{1}{2}\sigma_3(r_2 q_x + r_4 q_y)$, where σ_0, σ_1, σ_3 are three Pauli matrices and r_i, $i = 1, 2, ..., 6$ are six real parameters. The nodal structure for this LBC is obviously a nodal point, as expected.

B. Nodal structure and chiral symmetry

By all the 165 explicit $k \cdot p$ models enough to characterize the LBCs in the 80 LGs, we solve for the nodal structure that emanates from the LBC composed of k points (in the neighborhood of the LBC) at which the degeneracy of the LBC (2 or 4) is still preserved, and find that the nodal structure can be simply an isolated point, expressed by $q_x = 0, q_y = 0$ (which is simply the position where the LBC is located) or a line ($q_y = cq_x$ or $q_x = cq_y$, c is a real parameter) (see Table IV), as schematically depicted in Fig. 1. We note that the LBC within an HSPL is always twofold and the nodal structure is definitely a nodal line lying in the BZ. The characteristics of nodal structures for LBCs located in HSPs and HSLs are detailed below.

The Weyl LBC at HSP can appear in the four settings and the nodal structure can be a nodal point or nodal line. The Dirac LBC at the HSP can appear in the NTRS, SOC; TRS, NSOC; and TRS, SOC settings: In most cases, the nodal structure is a nodal point, while in the TRS, SOC setting, the nodal structure can also be a nodal line. The LBC in the HSL can be composed of one (co)irrep or two different (co)irreps. In the former case, the nodal structure is a nodal line along this HSL and such an LBC can appear in the four settings when its degeneracy is 2, while it can only appear in the TRS, SOC setting when the degeneracy is 4. In the latter case, the degeneracy of the LBC can be 2 (which can appear in the four settings) and the nodal structure can be a nodal point or nodal line (not parallel to the HSL). When the degeneracy is 4, the

TABLE IV. The list of all possible nodal structures emanating from LBCs at HSP, HSL, and HSPL. In the first column, the location of the LBC can be HSP, HSL, or HSPL. In the second column, the degeneracy of the LBC at HSP and HSL can be 2 or 4 while the degeneracy of the LBC at HSPL can only be 2. In the third column, nodal structures are separated by ";": $q_x = 0$, $q_y = 0$ stands for a nodal point, while $q_y = cq_x$ and $q_x = cq_y$ stand for nodal lines, where c can be a specific real number or expressed by real parameters r_1, r_2, r_3, r_4. Especially, when $c = 0$, the nodal line is $q_y = 0$ or $q_x = 0$. Note that the nodal structures are found based on explicit $k \cdot p$ models around the LBCs, and only one LBC is considered among symmetry-related LBCs for an LG in some setting.

Location of LBC	Degeneracy	Nodal structure
HSP	2	$q_x = 0, q_y = 0;\ q_x = 0;\ q_y = 0;\ q_y = \frac{r_1 q_x}{r_2};\ q_y = \frac{r_2 q_x}{r_1};\ q_y = -\frac{r_2 q_x}{r_1}$
	4	$q_x = 0, q_y = 0;\ q_x = 0;\ q_y = 0$
HSL	2	$q_x = 0, q_y = 0;\ q_x = 0;\ q_y = 0;\ q_y = q_x;\ q_y = -q_x;\ q_y = \frac{q_x}{\sqrt{3}};\ q_y = -\sqrt{3}q_x;\ q_y = -\frac{r_4 q_x}{r_3}$
	4	$q_x = 0, q_y = 0;\ q_x = 0;\ q_y = 0$
HSPL	2	$q_y = \frac{r_4 q_x}{r_3};\ q_y = -\frac{r_4 q_x}{r_3};\ q_y = \frac{r_3 q_x}{r_4};\ q_y = -\frac{r_3 q_x}{r_4}$

TABLE V. The list of LGs and concrete k points which necessarily host LBCs in the four settings. In the first column, NTRS (TRS) and NSOC (SOC) represent settings without (with) TRS and neglecting (considering) SOC, respectively. In the second column, the number before parentheses represents an LG number or several LGs (separated by comma), and the numbers (ranging from 1 to 25) in the parentheses encode the k points hosting essential LBCs in the corresponding LG(s): 1: $(0, 0)$, 2: $(\frac{1}{2}, \frac{1}{2})$, 3: $(\frac{1}{2}, -\frac{1}{2})$, 4: $(-\frac{1}{2}, \frac{1}{2})$, 5: $(-\frac{1}{2}, 0)$, 6: $(\frac{1}{2}, 0)$, 7: $(1, 0)$, 8: $(0, -\frac{1}{2})$, 9: $(0, \frac{1}{2})$, 10: $(\frac{1}{2}, w)$, 11: $(-\frac{1}{2}, w)$, 12: $(\frac{1}{2}, -w)$, 13: $(w, \frac{1}{2})$, 14: $(-w, \frac{1}{2})$, 15: $(w, -\frac{1}{2})$, 16: $(w, 0)$, 17: $(-w, 0)$, 18: $(0, w)$, 19: $(0, -w)$, 20: (w, w), 21: $(0, 2w)$, 22: $(2w, 0)$, 23: $(-w, 2w)$, 24: $(\frac{1}{2}, -v)$, 25: $(\frac{1}{2}, u)$, where the coordinates of the k points are given on the basis of reciprocal lattice basis vectors corresponding to the conventional real-space lattice. We use three colors: blue, red, and green to denote the degeneracy: When a k point (for an LG and a setting) can only necessarily host twofold degenerate Weyl LBCs, can only necessarily host fourfold degenerate Dirac LBCs, or can host both twofold degenerate Weyl LBCs [they are composed of one (co)irrep of dimension 2, and they necessarily appear] and fourfold degenerate Dirac LBCs [they are composed of two different (co)irreps of dimension 2, thus they do not necessarily appear], the number representing the k point is printed in blue, red, and green, respectively. In addition, when a number in parentheses is underlined, it means that the $k \cdot p$ model around each LBC in the corresponding k point can be uniquely determined by the degeneracy: When the LBC is twofold (fourfold) degenerate, the $k \cdot p$ model can only take one of those listed in Table SI2 of SM I [91].

Setting	LBCs that necessarily appear
NTRS, NSOC	7(2, 5) 15(3, 6) 16(3, 8) 17(6, 8) 20(2, 6) 21(6, 9) 24(3, 6) 25(6, 9) 31, 32, 33, 34, 38(2, 6, 10) 39(6, 9, 10, 13) 40(4, 5) 41(4, 5, 11) 42(6, 9, 10, 13) 43(3, 6, 8, 12) 44(6, 9) 45(2, 6, 9, 10) 46(6, 9, 10, 13) 48(2) 52(9) 54(6) 56, 58, 60(9) 62(9, 13) 63(9) 64(9, 13)
NTRS, SOC	7(2, 5) 15(3, 6) 16(3, 8) 17(6, 8) 19(1, 2, 6, 9) 20(1, 9) 21(1, 2) 22(1, 7) 23(1, 2, 6, 9) 24(1, 8) 25(1, 2) 26(1, 7) 27, 28, 29, 30(1, 2, 6, 9, 10, 18) 31, 32, 33, 34(1, 9, 18) 35, 36(1, 7, 21) 37(10, 13, 16, 18) 38(2, 6, 13, 16, 18) 39(2, 6, 9, 16, 18) 40(11, 14, 17, 18) 41(4, 5, 14, 17, 18) 42(6, 9, 16, 18) 43(3, 6, 15, 16, 19) 44(10, 13, 16, 18) 45(2, 6, 13, 16, 18) 46(2, 6, 9, 16, 18) 47(21, 22) 48(2, 21, 22) 52(9) 53(1, 2, 9) 54(1, 3) 55(1, 2, 9) 56(1, 2) 57(1, 2, 9) 58(1, 2) 59(1, 2, 9) 60(1, 2) 61(13, 18, 20) 62(2, 9, 18, 20) 63(13, 18, 20) 64(2, 9, 18, 20) 76, 77(9) 78(9, 18) 79(9, 23) 80(18, 23)
TRS, NSOC	5, 7(2, 5) 9(3, 6, 24) 12(3, 8, 15) 15(3, 6, 24) 16(3, 8, 15) 17(6, 8, 15, 25) 20(2, 6, 10) 21(6, 9, 10, 13) 24(3, 6, 12) 25(6, 9, 10, 13) 28(2, 9, 13) 29(2, 9, 13) 30(2, 9, 13) 31(2, 6, 10) 32(6, 9, 10, 13) 33(2, 6, 9, 10, 13) 34(6, 9, 10, 13) 36(2) 38(2, 6, 10) 39(6, 9, 10, 13) 40(4, 5, 11) 41(4, 5, 11) 42(6, 9, 10, 13) 43(3, 6, 8, 12, 15) 44(6, 9, 10, 13) 45(2, 6, 9, 10, 13) 46(6, 9, 10, 13) 48(2) 52(9) 54(6, 12) 56, 58, 60, 62(9, 13) 63(9, 13) 64(9, 13)
TRS, SOC	1(1, 2, 6, 9) 3, 4(1, 2, 6, 8) 5(1, 2, 5, 9) 7(2, 5) 8(1, 3, 6, 8) 9(1, 3, 6, 8, 24) 10(1, 3, 7) 11(1, 3, 6, 8) 12(1, 3, 6, 8, 15) 13(1, 3, 7) 15(3, 6) 16(3, 8) 17(6, 8) 19(1, 2, 6, 9) 20(1, 2, 6, 9, 10) 21(1, 2, 6, 9, 10, 13) 22(1, 2, 7) 23(1, 2, 6, 9) 24(1, 3, 6, 8, 12) 25(1, 2, 6, 9, 10, 13) 26(1, 2, 7) 27(1, 2, 6, 9, 10, 18) 28(1, 2, 6, 9, 10, 13, 18) 29(1, 2, 6, 9, 10, 13, 18) 30(1, 2, 6, 9, 10, 13, 18) 31(1, 2, 6, 9, 18) 32(1, 2, 6, 9, 13, 18) 33(1, 2, 6, 9, 13, 18) 34(1, 2, 6, 9, 13, 18) 35, 36(1, 2, 7, 21) 38(2, 6) 39(2, 6, 9) 40(4, 5, 11) 41(4, 5) 42(6, 9) 43(3, 6, 8, 15) 44(6, 9, 10, 13) 45(2, 6, 9, 13) 46(2, 6, 9) 48(2) 49, 50(1, 2, 9) 52(2, 9) 53(1, 2) 54(1, 3, 6, 12) 55(1, 2, 9) 56(1, 2, 9, 13) 57(1, 2, 9) 58(1, 2, 9, 13) 59(1, 2, 9) 60(1, 2, 9, 13) 62(2, 9) 63(9, 13) 64(2, 9) 65, 67, 68, 69, 70, 73, 74, 76, 77(9) 78(9, 18) 79(9, 23)

nodal structure is definitely a nodal point and the LBC can only appear in the TRS, NSOC and TRS, SOC settings.

It is worth pointing out that the nodal structures (a nodal point and nodal line) can be partially deduced from the compatibility relations [82]: Once the nodal point solution from the $k \cdot p$ model of some LBC is found, the LBC is thus definitely a nodal point, also required by the compatibility relations. However, once a nodal line solution is found, it might be gapped by including higher-order $k \cdot p$ term(s), leaving a strictly nodal point by the compatibility relations, in which sense the nodal line by our $k \cdot p$ model (expanded only to the first order) is a nearly nodal structure. Interestingly, there exists a nodal line that cannot be captured by the compatibility relations. Such a nodal line is protected by mirror symmetry and can be found by the constructed $k \cdot p$ model.

In addition, we also solve for the possible chiral symmetry given the explicit $k \cdot p$ model. The chiral symmetry operation C should satisfy that $CH_i(\vec{q})C^\dagger = -H_i(\vec{q})$ (where H_i is one of the 165 $k \cdot p$ models and $\dagger$ denotes the Hermitian conjugation), and thus we find that 78 of the 165 models allow a chiral symmetry, as shown in Table SI2 of SM I [91]. Note that the chiral symmetry found is approximate in the sense that it is only satisfied when the $k \cdot p$ model is expanded to the linear order and can be broken when considering higher order term(s) of $\vec{q}$. The existence of the chiral symmetry in the low-energy model enforces symmetry constraints beyond those by crystallographic symmetries and the complete list of the possible chiral symmetries can be applied for further theoretical studies and materials prediction.

III. LBCS ENFORCED TO APPEAR NECESSARILY

Next, we highlight the LBCs that are enforced or guaranteed to appear essentially or necessarily in the 80 LGs: First, such kind of LBC should contain only one (co)irrep since LBCs composed of two different (co)irreps usually need an accidental band inversion; Second, any (co)irrep of the k point hosting the LBC contributes to one LBC. In this way, we tabulate in Table V all the k points and LGs for the four settings, where the LBC necessarily appears. In Table V, the k point (represented by an integer) is in blue, red, or green, when it only necessarily hosts a Weyl LBC, only necessarily hosts a Dirac LBC, or hosts both types of LBCs, respectively. When the $k \cdot p$ model can be uniquely determined by the degeneracy

TABLE VI. All the LBCs in LG 15 with TRS as listed in SM I [91]. The LBCs are packaged according to the k points hosting them and each k point corresponds to four rows for a given setting: We first provide the coordinate of the k point in the first row (indicated by k) whose coordinate is expressed on the basis vectors of reciprocal lattice corresponding to the conventional lattice. Then, in the second row, we provide the little group $G(k)$: The operations g_1, g_2, g_3, g_4 can be found in Sec. IV while Θ denotes the time-reversal operation. We only provide one antiunitary operation (combination of Θ and a spatial operation) once $G(k)$ contains antiunitary operations. In the third row, for each LBC in the k point, we provide the representation matrices (RepM) and the corresponding $k \cdot p$ model ($H_{k\cdot p}$). The representation matrices in the form of R_i are provided in Table SI1 of SM I [91] while the $k \cdot p$ models in the form of H_i can be found in Table SI2 of SM I [91]. In the fourth row, we provide all operations (β) that relate other LBCs with the listed LBC. The $k \cdot p$ models around the β-related LBCs can be deduced by β and the listed $k \cdot p$ model (see SM I [91]). In addition, the color coding on the k point and representation matrix are described as follows. The k point is printed in blue and red, when it can only necessarily host twofold degenerate Weyl LBCs, and can only necessarily host fourfold degenerate Dirac LBCs. For HSL, when the LBC contains only one (co)irrep, the corresponding representation matrices are printed in cyan.

LBCs in LG 15 in the TRS, NSOC setting

k	$(\frac{1}{2}, 0)$	$(\frac{1}{2}, -\frac{1}{2})$	$(w, 0)$
$G(k)$	$g_1, g_2, g_3, g_4, \Theta g_1$	$g_1, g_2, g_3, g_4, \Theta g_1$	$g_1, g_2, \Theta g_3$
RepM : $H_{k\cdot p}$	$R_{35}, R_{11}, R_{34}, R_9, R_{35} : H_{25}$	$R_{35}, R_{11}, R_{34}, R_9, R_{35} : H_{25}$	$R_{35}, R_{34}, R_{35} : H_{21}$
β	g_1	g_1	g_1, g_3
k	$(w, -\frac{1}{2})$	$(\frac{1}{2}, -v)$	$(0, -v)$
$G(k)$	$g_1, g_2, \Theta g_3$	$g_1, g_4, \Theta g_2$	$g_1, g_4, \Theta g_2$
RepM : $H_{k\cdot p}$	$R_{35}, R_{34}, R_{35} : H_{21}$	$R_{35}, R_{27}, R_8 : H_{26}$	$R_{35}, R_{34}, R_{35} : H_{22}$
β	g_1, g_3	g_1, g_2	g_1, g_2

LBCs in LG 15 in the TRS, SOC setting

k	$(\frac{1}{2}, 0)$	$(\frac{1}{2}, -\frac{1}{2})$	$(\frac{1}{2}, -v)$
$G(k)$	$g_1, g_2, g_3, g_4, \Theta g_1$	$g_1, g_2, g_3, g_4, \Theta g_1$	$g_1, g_4, \Theta g_2$
RepM : $H_{k\cdot p}$	$R_{114}, R_{97}, R_{112}, R_{92}, R_{71} : H_{117}$	$R_{114}, R_{97}, R_{112}, R_{92}, R_{71} : H_{117}$	$R_{114}, R_{113}, R_{69} : H_{118}$
β	g_1	g_1	g_1, g_2

(2 or 4), the integer for this k point is then underlined. See Table SI578 in SM I [91] for an example, where three LBCs can be found (the degeneracies are 2, 2, and 4, respectively): In Table SI578 in SM I [91], the two twofold degenerate LBCs share one common $k \cdot p$ model (namely, H_{56}) while the fourfold degenerate LBC owns the $k \cdot p$ model being H_{124}; thus, directly by the degeneracy of an LBC, the $k \cdot p$ model can be uniquely determined (namely, H_{56} or H_{124} for LBCs with degeneracy 2 or 4, respectively). Table V is expected to speed up the materials searches since the existence of LBCs can be inferred directly from the materials structure symmetry without any realistic calculations, as we will demonstrate in the materials investigation on a 2D materials database (2DMatPedia) [40] in Sec. V. In SM I [91], we have also printed the coordinate of the k point in red, blue, and green to convey the same information as above.

IV. EXAMPLE: LBCS IN LG 15

Before an application to materials database investigation, we take LG 15 with TRS as an example to demonstrate how to use SM I [91] to quickly obtain all possible LBCs. First, LG 15 owns a simple rectangle lattice, which can be known by the Cartesian coordinates of the conventional lattice basis vectors $\vec{a}, \vec{b}, \vec{c}$ and the transformation matrix A_{cp} from $\vec{a}, \vec{b}, \vec{c}$ to $\vec{a}_1, \vec{a}_2, \vec{a}_3$ in the beginning of Sec. SI2.15 of SM I [91]. The representative operations of the left coset, LG 15 with respect to the translation group generated by $\vec{a}_1, \vec{a}_2, \vec{a}_3$, are also listed there: $g_1 = (x, y, z)$, $g_2 = (x + \frac{1}{2}, -y, -z)$, $g_3 = (-x, -y, -z)$, $g_4 = (\frac{1}{2} - x, y, z)$, where g_3 is the inversion operation, and thus the electronic bands own Kramers degeneracy for all k points in the TRS, SOC setting. Note that g_2 is a screw operation, responsible for the larger band degeneracy occurring in the BZ boundary compared with that in the BZ interior. By Sec. SI2.15.c and Sec. SI2.15.d of SM I [91], relevant for LBCs for the TRS, NSOC and TRS, SOC settings, respectively, containing several tables, each of which correspond to one (independent) k point, we know all LBCs in LG 15 with TRS, as listed in Table VI for the collection of all these tables.

By Table VI, we know that all possible $k \cdot p$ models for the LBCs of LG 15 with TRS are $H_{21} = q_x(r_1\sigma_0 + r_2\sigma_3) + r_3q_y\sigma_1$, $H_{22} = q_y(r_1\sigma_0 + r_2\sigma_3) + r_3q_x\sigma_2$, $H_{25} = r_1q_x\sigma_2$, $H_{26} = q_x(r_1\sigma_1 + r_2\sigma_2) + r_3q_y\sigma_0$ and $H_{117} = r_1q_y\sigma_0\sigma_2 + q_x(r_2\sigma_1\sigma_1 + r_3\sigma_2\sigma_1 + r_4\sigma_3\sigma_1)$, $H_{118} = r_1q_y\sigma_0\sigma_0 + q_x(r_2\sigma_1\sigma_1 + r_3\sigma_1\sigma_2 + r_4\sigma_1\sigma_3) + r_6q_y\sigma_3\sigma_0$ ($\sigma_0, \sigma_1, \sigma_2, \sigma_3$ are four Pauli matrices, $r_1, r_2, \ldots, r_6$ are all real parameters, which can be determined by concrete materials structure, and $\sigma_\mu\sigma_\nu$ means a direct product $\sigma_\mu \otimes \sigma_\nu$). Besides, all possible representation matrices of little groups for LBCs of LG 15 with TRS are $R_8 = -\mathrm{i}\sigma_2, R_9 = -\mathrm{i}\sigma_1, R_{11} = -\sigma_2, R_{27} = -\mathrm{i}\sigma_3, R_{34} = \sigma_3, R_{35} = \sigma_0$ and $R_{69} = -\mathrm{i}\sigma_0\sigma_2, R_{71} = -\mathrm{i}\sigma_2\sigma_0, R_{92} = \sigma_0\sigma_2, R_{97} = \mathrm{i}\sigma_0\sigma_1, R_{112} = \sigma_0\sigma_3, R_{113} = \sigma_3\sigma_9, R_{114} = \sigma_0\sigma_0$ (i is the imaginary unit). Note that for all 2183 LBCs, there are 127 matrices in the form of $R_i (i = 1, 2, \ldots 127)$, provided in Table SI1 of SM I [91]. Note that the LBC lying in the HSLs can be composed of one coirrep or two different coirreps. In SM I [91], for the HSL, we have printed the representation matrices in cyan when the corresponding LBC contains only one (co)irrep. For the LBCs of LG 15 with TRS, all the LBCs in the HSLs listed in Table VI contain two coirreps except the LBC in the HSL $(\frac{1}{2}, -v)$ in the TRS, NSOC

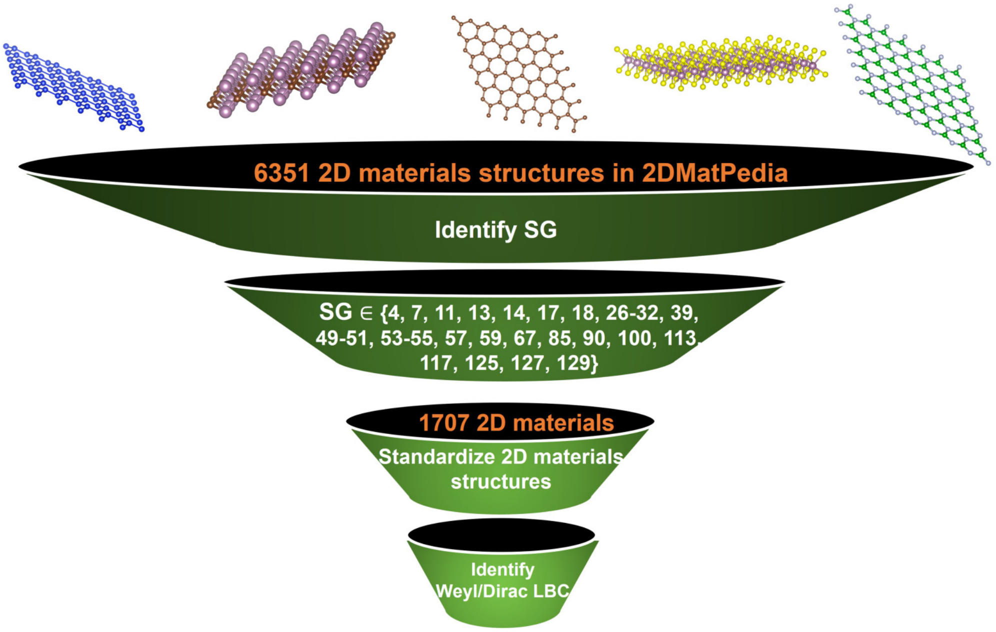

FIG. 2. Work flow of predicting 2D materials with Weyl (Dirac) LBCs coexisting in both electronic and phononic band structures. Each of the 6351 2D materials structures cataloged in 2DMatPedia can be assigned by an SG number by VASPKIT. There are 1707 structures whose SGs belong to the 32 SGs, whose LGs necessarily host coexisting spinless and spinful LBCs. The last step is to quantitatively identify the LBCs in the first-principles calculated electronic and phononic band structures, which require the structures to be standardized, namely, the structures should be invariant upon the LG operations, as listed in SM I.

setting which contains only one coirrep (the $k \cdot p$ model for this LBC is H_{26}, whose nodal structure is $q_x = 0$ along the HSL while the rest of the LBCs in the HSLs are nodal points since the nodal structures by the explicit $k \cdot p$ models, H_{21}, H_{22}, and H_{118} are $q_x = 0, q_y = 0$). Note that the LBC in the HSL composed of two different (co)irreps can also be a nodal line. For example, there are six LBCs in HSL $(w, 0)$ in LG 39 in the TRS, NSOC setting, all composed of two different (co)irreps, and the $k \cdot p$ models can be $H_{33} = r_1 q_x \sigma_0 + r_2 q_y \sigma_1 + r_3 q_x \sigma_3$ or $H_{51} = r_1 q_x \sigma_0 + r_2 q_x \sigma_3$, whose nodal structure is $q_x = 0, q_y = 0$ (a nodal point) or $q_x = 0$ (a nodal line perpendicular to this HSL), respectively.

V. MATERIALS INVESTIGATION

We then perform a materials investigation for 2D materials based on our results. The 6351 2D materials structures in 2DMatPedia [40] are used, of which around 50 structures have been experimentally synthesized. Note that first-principles calculations on 2D materials usually adopt a three-dimensional (3D) structure (with the length perpendicular to the 2D material set very large). The SG, rather than LG, for the 3D structure, can be identified conveniently, for example, by VASPKIT [97]. Though one SG might correspond to two different LGs as shown in Table VII, it is interesting to find that both LGs can necessarily host LBCs. Here we are concerned with two types of necessarily existing LBCs: One is for the necessarily coexisting spinful and spinless LBCs, denoted by green in Table VII, while the other is for necessarily and only necessarily existing spinful LBCs, denoted by red in Table VII. Note that necessarily and only necessarily existing spinless LBCs cannot occur from our results.

Following the work flow shown in Fig. 2, we can obtain 1707 2D materials hosting coexisting LBCs in both electronic and phononic band structures in one sweep: The 32 SGs for the 37 LGs: LGs 5, 7, 9, 12, 15-17, 20, 21, 24, 25, 28-34, 36, 38-46, 48, 52, 54, 56, 58, 60, 62-64 as printed in green in Table VII considering TRS are utilized. In a similar way, we also obtain 3035 2D materials necessarily and only necessarily hosting electronic LBCs, based on SGs for the LGs printed in red in Table VII with TRS. All the 1707 and 3035 2D materials are provided in SM II [92]. We choose 66 2D materials to demonstrate the coexisting electronic and phononic LBCs by first-principles calculations and the results are displayed in SM II [92]. In the following, we choose Zr_2HBr_2 in LG 15 to illustrate. It is worth pointing out that the LBCs in these 2D materials have been required to exist by structure symmetry, without performing realistic calculations [98].

Zr_2HBr_2 in LG 15: Coexisting electronic Dirac point and phononic Weyl nodal line

Zr_2HBr_2 is crystallized in LG 15 with a simple rectangle lattice (the material ID in 2DMatPedia [40] is mp-642803), and the first-principles calculated electronic and phononic band structures are shown in Figs. 3(a) and 3(c), respectively. The four HSPs are $\Gamma = (0, 0), X = (\frac{1}{2}, 0), S = (\frac{1}{2}, \frac{1}{2})$, and $Y = (0, \frac{1}{2})$. By Table VI, we can know that X and S can host Weyl LBC in the phononic bands and Dirac LBC in the electronic bands. Furthermore, according to Table V, these LBCs at their HSPs exist necessarily, and the corresponding $k \cdot p$

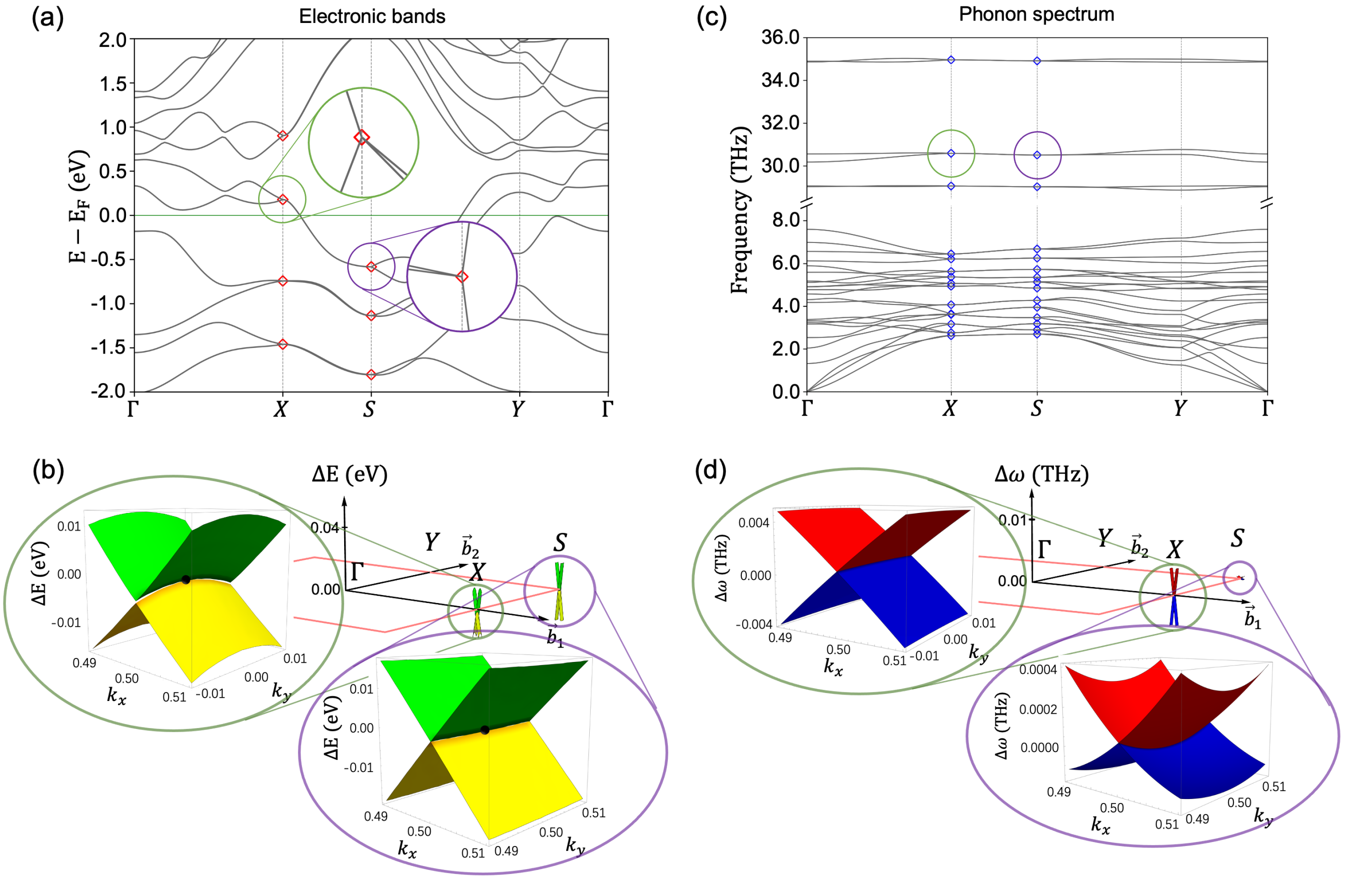

FIG. 3. The electronic and phononic band structures of Zr_2HBr_2 in LG 15. In (a) and (c), the electronic and phoninic bands along high-symmetry k paths are depicted, respectively, where the necessarily existing Dirac and Weyl LBCs are indicated by red and blue diamonds, respectively. Around the LBCs inside the circles as shown in (a) and (c), we plot the low-energy band structures in (b) and (d), respectively: ΔE ($\Delta\omega$) is defined to be the difference of energy (frequency) and that of the LBC. These low-energy band structures are consistent with the $k \cdot p$ models: The LBCs in (a) are all Dirac nodal points, and the bands would split in any direction away from the LBCs. The LBCs in (c) lie in nodal lines along XS. In addition, all the low-energy bands in (b) and (d) display an approximate particle-hole symmetry.

models can be uniquely determined simply by the degeneracy. Concretely, the $k \cdot p$ models for the Weyl LBCs in X and S in the phononic bands are all H_{25}, while the $k \cdot p$ models for the Dirac LBCs in X and S in the electronic bands are all H_{117}. By H_{117}, the Dirac LBCs are nodal points in the electronic bands, as shown in Fig. 3(b). By H_{25}, the Weyl LBCs actually lie in a nodal line $q_x = 0$ along XS, as shown in Fig. 3(d). The Weyl nodal line emanating from the Weyl LBC by H_{25} can also be anticipated by H_{26}, which characterizes the $k \cdot p$ models around all Weyl LBCs with XS based on Table VI. Since LG 15 contains I symmetry (I: spatial inversion), the Berry curvatures are all vanishing by ΘI throughout the BZ. It can be expected to induce large Berry curvatures by external perturbations breaking ΘI symmetry starting from this material.

To verify the correctness of the constructed $k \cdot p$ model, we demonstrate the comparison of the energy contours for the electronic band structures near the Dirac points at X and S for Zr_2HBr_2. As shown in Figs. 4(a) and 4(b), the energy contours are chosen to be for $\Delta E = -0.01/-0.005/-0.001/-0.0005/-0.0001$ eV and $\Delta E = 0.01/0.005/0.001/0.0005/0.0001$ eV, respectively, at X. ΔE denotes the energy difference of the energy and that for the Dirac point in the green circle [Fig. 3(a)]. We can find that the energy contours obtained by the $k \cdot p$ model and from the first-principles results fit very well when they are close to the Dirac point, but the deviation becomes larger with increasing $|\Delta E|$. In addition, for the Dirac point [in the purple circle in Fig. 3(a)] at S, the energy contours by the $k \cdot p$ model and from the first-principles results for all the chosen values of ΔE fit very well. The different fitting qualities of the band structures for the Dirac points at X and S can be owed to the effect of higher order $k \cdot p$ terms. It is found that adding $k \cdot p$ terms proportional to q^2 indeed improves the fitting quality of the energy contours for the Dirac points around X for all chosen values of ΔE.

VI. METHOD

Based on the 1707 obtained 2D materials definitely hosting coexisting electronic and phononic LBCs, we first select 167 materials to perform first-principles calculations: The number of atoms per unit cell should be $\leqslant 10$ and materials containing typical magnetic ions and materials with

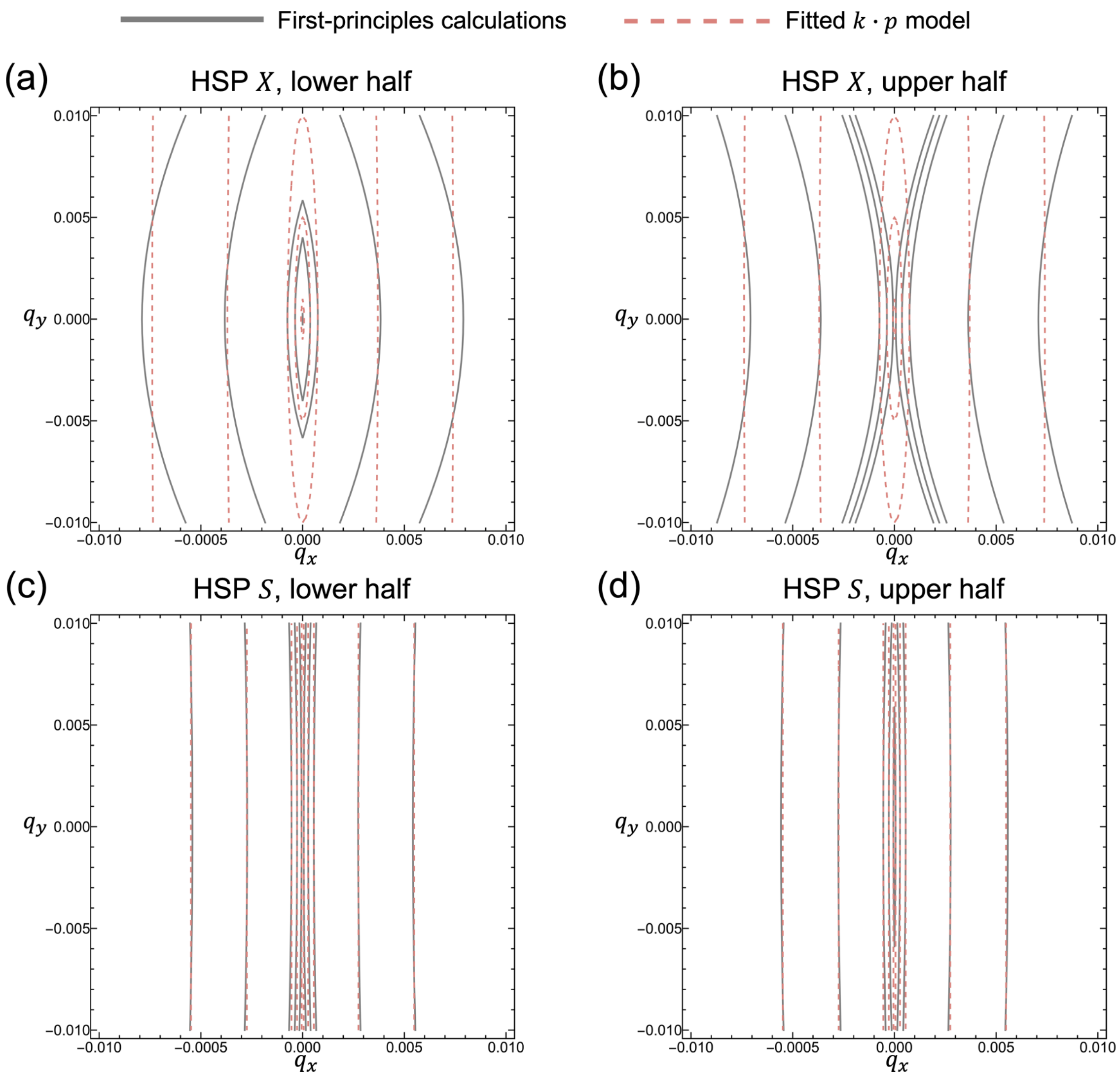

FIG. 4. Comparison of the electronic energy contours around the Dirac points in Fig. 3(a) [which are indicated by the green (purple) circle] by the fitted $k \cdot p$ model at HSP X/S and by the first-principles calculations for Zr_2HBr_2. The $k \cdot p$ model for the Dirac point in X or S is $H_{117} = r_1\gamma_{02}(-q_y) + r_2\gamma_{11}q_x + r_3\gamma_{21}q_x + r_4\gamma_{31}q_x$, which contains four real parameters to be determined. For the Dirac point at X, the fitted parameters are found to be $r_1 = 0.1$ eV, $r_2 = 0.814678$ eV, $r_3 = 0.902539$ eV, and $r_4 = 0.5922$ eV. For the Dirac point at S, the fitted parameters are $r_1 = 0.0021$ eV, $r_2 = 1.518167$ eV, $r_3 = 0.008725$ eV, and $r_4 = 1.008725$ eV. The energy contours are for different values of ΔE, which is defined to be the difference of energy and that of the Dirac point: The energy contours for $\Delta E = -0.01/-0.005/-0.001/-0.0005/-0.0001$ eV (the lower half in the figure) are shown in (a) and (c) for X and S, respectively. The energy contours for $\Delta E = 0.01/0.005/0.001/0.0005/0.0001$ eV (the upper half in the figure) are shown in (b) and (d) for X and S, respectively. In each panel, the absolute value of ΔE gradually increases from the inside to the outside.

duplicate chemical formula are filtered out. We obtain 66 materials which have no imaginary frequencies or whose imaginary frequencies are $\leqslant$ 0.5 THz. The first-principles calculation in this work is based on the density functional theory implemented in the VIENNA AB-INITIO SIMULATION PACKAGE (VASP) [99,100] using the projector augmented wave method [101]. The generalized gradient approximation [102] in the form of the Perdew-Burke-Enzerhof scheme is adopted for the exchange and correlation functional [103]. The plane-wave energy cutoff is set to 1.5 times the default cutoff energy in all calculations. For the self-consistent calculation of the electronic ground state, the gamma-centered Monkhorst-Pack scheme for BZ sampling is generated using the VASPKIT package [97] with accuracy of 0.02 $2\pi/\text{Å}$. The convergence criterion of the self-consistent calculation is set at 10^{-8} eV. SOC is considered in the electronic calculations. In the calculations of phonons, SOC is not included and the PHONOPY package [104] is used to compute the phonon spectra.

VII. CONCLUSION AND DISCUSSION

It is worth pointing out that though Refs. [82,86] have already been concerned with the band crossings for the 528

TABLE VII. The correspondence from SG to LG(s) and LGs allowing LBCs to necessarily exist considering only NSOC (SOC) and considering both NSOC and SOC with TRS (without TRS). The LG number in red means that LBC necessarily exists only in the TRS, SOC(NTRS, SOC) setting in this LG. The LG number in green means that LBC necessarily exists in both the TRS, SOC and TRS, NSOC settings (or in both the NTRS, SOC and NTRS, NSOC settings) in this LG. Note that there is no LG in which LBC necessarily exists only in the TRS, NSOC setting (only in the NTRS, NSOC setting).

Necessarily coexisting spinful and spinless LBCs with TRS																								
SG	1	2	3	4	5	6	7	8	10	11	12	13	14	16	17	18	21	25	26	27	28	29	30	31
LG	1	2	3, 8	9	10	4, 11	5, 12	13	6, 14	15	18	7, 16	17	19	20	21	22	23, 27	28, 29	30	24, 31	33	34	32
SG	32	35	38	39	47	49	50	51	53	54	55	57	59	65	67	75	81	83	85	89	90	99	100	111
LG	25	26	35	36	37	38	39	40, 41	42	43	44	45	46	47	48	49	50	51	52	53	54	55	56	57
SG	113	115	117	123	125	127	129	143	147	149	150	156	157	162	164	168	174	175	177	183	187	189	191	
LG	58	59	60	61	62	63	64	65	66	67	68	69	70	71	72	73	74	75	76	77	78	79	80	
Necessarily coexisting spinful and spinless LBCs without TRS																								
SG	1	2	3	4	5	6	7	8	10	11	12	13	14	16	17	18	21	25	26	27	28	29	30	31
LG	1	2	3, 8	9	10	4, 11	5, 12	13	6, 14	15	18	7, 16	17	19	20	21	22	23, 27	28, 29	30	24, 31	33	34	32
SG	32	35	38	39	47	49	50	51	53	54	55	57	59	65	67	75	81	83	85	89	90	99	100	111
LG	25	26	35	36	37	38	39	40, 41	42	43	44	45	46	47	48	49	50	51	52	53	54	55	56	57
SG	113	115	117	123	125	127	129	143	147	149	150	156	157	162	164	168	174	175	177	183	187	189	191	
LG	58	59	60	61	62	63	64	65	66	67	68	69	70	71	72	73	74	75	76	77	78	79	80	

magnetic layer groups, we focus our attention on the LBCs in the 80 LGs in the four settings, list all symmetry-related LBCs and also adopted a different convention as adopted in the Bilbao server, which has been adopted as the default convention in many famous software [74,97,105]. By the explicit $k \cdot p$ models around the LBCs, we also find all possible nodal structures and approximate chiral symmetries. Several useful rules that guarantee the LBCs to appear as shown in Tables V and VII are established. Different from simply a group-theoretical classification in Refs. [82,86], we perform material predictions for the LBCs in 2D materials by first-principles calculations.

To conclude, we perform large-scale symmetry analysis on all LBCs that can appear in the 80 LGs in four different symmetry settings with (without) TRS and in the spinless (spinful) settings. All possible positions, including HSPs, HSLs, and HSPLs are scanned to obtain a complete list of all LBCs in the 80 LGs. In total, we collect 2183 independent LBCs with 165 different $k \cdot p$ models. It is worth pointing out that, for any of 2183 LBCs, we provide all other symmetry-related LBCs and their $k \cdot p$ models, suitable for the study of valley-related low-energy physics. We also provide the representation matrices for each LBC.

Other than tabulating all LBCs by the 80 LGs, we also provide useful hints for materials searches. First, we highlight k points necessarily hosting LBC and list LGs necessarily hosting LBCs coexisting in the spinless and spinful settings. Second, it is interesting to find that one can directly utilize the information of SG for 2D material (SG can be obtained by restoring the translation symmetry in the direction perpendicular to the 2D material) to determine whether it necessarily hosts spinful (spinless) LBCs, which is practically convenient in the first-principles calculation.

Finally, the 17 wallpaper groups, namely, LGs 1, 3, 11–13, 23–26, 49, 55, 56, 65, 69, 70, 73, and 77, can characterize symmetries of surfaces of three-dimensional crystals and 2D materials grown on a substrate. The emergent Dirac wallpaper fermions have been proposed in Ref. [25], which can be realized in surfaces owning the *pgg* or *p*4*g* wallpaper group (LG 25 or LG 56, respectively) of topological crystalline insulators, consistent with the Dirac LBCs for LGs 25 and 26 revealed in this paper. We expect the results in this work can act as a basis for further exploration on the effects of symmetry-breaking perturbation (e.g., the modification of the topological character, the number of the symmetry-related LBCs, and the band dispersion around the LBC) in a large-scale way based on the 80 LGs.

ACKNOWLEDGMENTS

This paper was supported by the National Natural Science Foundation of China (NSFC) under Grants No. 12188101, No. 12322404, No. 12104215, No. 11834006, the National Key R&D Program of China (Grant No. 2022YFA1403601), and Innovation Program for Quantum Science and Technology, No. 2021ZD0301902. F.T. was also supported by the Young Elite Scientists Sponsorship Program by the China Association for Science and Technology. X.W. also acknowledges support from the Tencent Foundation through the XPLORER PRIZE.

[1] K. S. Novoselov, A. K. Geim, S. V. Morozov, D. Jiang, Y. Zhang, S. V. Dubonos, I. V. Grigorieva, and A. A. Firsov, Electric field effect in atomically thin carbon films, Science **306**, 666 (2004).

[2] A. H. Castro Neto, F. Guinea, N. M. R. Peres, K. S. Novoselov, and A. K. Geim, The electronic properties of graphene, Rev. Mod. Phys. **81**, 109 (2009).

[3] M. I. Katsnelson, K. S. Novoselov, and A. K. Geim, Chiral tunnelling and the Klein paradox in graphene, Nat. Phys. **2**, 620 (2006).

[4] C. Gutiérrez, L. Brown, C.-J. Kim, J. Park, and A. N. Pasupathy, Klein tunnelling and electron trapping in nanometre-scale graphene quantum dots, Nat. Phys. **12**, 1069 (2016).

[5] Y. Zhang, Y. Tan, H. L. Stormer, and P. Kim, Experimental observation of the quantum Hall effect and Berry's phase in graphene, Nature (London) **438**, 201 (2005).

[6] K. S. Novoselov, Z. Jiang, Y. Zhang, S. V. Morozov, H. L. Stormer, U. Zeitler, J. C. Maan, G. S. Boebinger, P. Kim, and A. K. Geim, Room-temperature quantum Hall effect in graphene, Science **315**, 1379 (2007).

[7] F. D. M. Haldane, Model for a quantum Hall effect without Landau Levels: Condensed-matter realization of the parity anomaly, Phys. Rev. Lett. **61**, 2015 (1988).

[8] M. Onoda and N. Nagaosa, Quantized anomalous Hall effect in two-dimensional ferromagnets: Quantum Hall effect in metals, Phys. Rev. Lett. **90**, 206601 (2003).

[9] R. Yu, W. Zhang, H.-J. Zhang, S.-C. Zhang, X. Dai, and Z. Fang, Quantized anomalous Hall effect in magnetic topological insulators, Science **329**, 61 (2010).

[10] C.-Z. Chang, J. Zhang, X. Feng, J. Shen, Z. Zhang, M. Guo, K. Li, Y. Ou, P. Wei, L.-L. Wang, Z.-Q. Ji, Y. Feng, S. Ji, X. Chen, J. Jia, X. Dai, Z. Fang, S.-C. Zhang, K. He, Y. Wang, L. Lu, X.-C. Ma, and Q.-K. Xue, Experimental observation of the quantum anomalous Hall effect in a magnetic topological insulator, Science **340**, 167 (2013).

[11] C. Wu, Orbital analogue of the quantum anomalous Hall effect in *p*-band systems, Phys. Rev. Lett. **101**, 186807 (2008).

[12] C. L. Kane and E. J. Mele, Z_2 topological order and the quantum spin Hall effect, Phys. Rev. Lett. **95**, 146802 (2005).

[13] C. L. Kane and E. J. Mele, Quantum spin Hall effect in graphene, Phys. Rev. Lett. **95**, 226801 (2005).

[14] B. A. Bernevig, T. L. Hughes, and S.-C. Zhang, Quantum spin Hall effect and topological phase transition in HgTe quantum wells, Science **314**, 1757 (2006).

[15] C.-C. Liu, W. Feng, and Y. Yao, Quantum spin Hall effect in silicene and two-dimensional germanium, Phys. Rev. Lett. **107**, 076802 (2011).

[16] X. Qian, J. Liu, L. Fu, and J. Li, Quantum spin Hall effect in two-dimensional transition metal dichalcogenides, Science **346**, 1344 (2014).

[17] A. Rycerz, J. Tworzydło, and C. W. J. Beenakker, Valley filter and valley valve in graphene, Nat. Phys. **3**, 172 (2007).

[18] D. Xiao, W. Yao, and Q. Niu, Valley-contrasting physics in graphene: magnetic moment and topological transport, Phys. Rev. Lett. **99**, 236809 (2007).

[19] D. Xiao, G.-B. Liu, W. Feng, X. Xu, and W. Yao, Coupled spin and valley physics in monolayers of MoS_2 and other group-VI dichalcogenides, Phys. Rev. Lett. **108**, 196802 (2012).

[20] I. Sodemann and L. Fu, Quantum nonlinear Hall effect induced by Berry curvature dipole in time-reversal invariant materials, Phys. Rev. Lett. **115**, 216806 (2015).

[21] Q. Ma, S.-Y. Xu, H. Shen, D. MacNeill, V. Fatemi, T.-R. Chang, A. M. M. Valdivia, S. Wu, Z. Du, C.-H. Hsu, S. Fang, Q. D. Gibson, K. Watanabe, T. Taniguchi, R. J. Cava, E. Kaxiras, H.-Z. Lu, H. Lin, L. Fu, N. Gedik, and P. Jarillo-Herrero, Observation of the nonlinear Hall effect under time-reversal-symmetric conditions, Nature (London) **565**, 337 (2019).

[22] Z. Z. Du, H.-Z. Lu, and X. C. Xie, Nonlinear Hall effects, Nat. Rev. Phys. **3**, 744 (2021).

[23] P. R. Wallace, The band theory of graphite, Phys. Rev. **71**, 622 (1947).

[24] S. M. Young and C. L. Kane, Dirac semimetals in two dimensions, Phys. Rev. Lett. **115**, 126803 (2015).

[25] B. J. Wieder, B. Bradlyn, Z. Wang, J. Cano, Y. Kim, H.-S. D. Kim, A. M. Rappe, C. L. Kane, and B. A. Bernevig, Wallpaper fermions and the nonsymmorphic Dirac insulator, Science **361**, 246 (2018).

[26] C. Le, Z. Yang, F. Cui, A. P. Schnyder, and C.-K. Chiu, Generalized fermion doubling theorems: Classification of two-dimensional nodal systems in terms of wallpaper groups, Phys. Rev. B **106**, 045126 (2022).

[27] K. S. Novoselov, D. Jiang, F. Schedin, T. J. Booth, V. V. Khotkevich, S. V. Morozov, and A. K. Geim, Two-dimensional atomic crystals, Proc. Natl. Acad. Sci. USA **102**, 10451 (2005).

[28] P. Vogt, P. De Padova, C. Quaresima, J. Avila, E. Frantzeskakis, M. C. Asensio, A. Resta, B. Ealet, and G. Le Lay, Silicene: Compelling experimental evidence for graphenelike two-dimensional silicon, Phys. Rev. Lett. **108**, 155501 (2012).

[29] M. Naguib, M. Kurtoglu, V. Presser, J. Lu, J. Niu, M. Heon, L. Hultman, Y. Gogotsi, and M. W. Barsoum, Two-dimensional nanocrystals produced by exfoliation of Ti_3AlC_2, Adv. Mater. **23**, 4248 (2011).

[30] C. Xu, L. Wang, Z. Liu, L. Chen, J. Guo, N. Kang, X.-L. Ma, H.-M. Cheng, and W. Ren, Large-area high-quality 2D ultrathin Mo_2C superconducting crystals, Nat. Mater. **14**, 1135 (2015).

[31] K. H. Lee, H.-J. Shin, J. Lee, I.-Y. Lee, G.-H. Kim, J.-Y. Choi, and S.-W. Kim, Large-scale synthesis of high-quality hexagonal boron nitride nanosheets for large-area graphene electronics, Nano Lett. **12**, 714 (2012).

[32] Y.-L. Hong, Z. Liu, L. Wang, T. Zhou, W. Ma, C. Xu, S. Feng, L. Chen, M.-L. Chen, D.-M. Sun, X.-Q. Chen, H.-M. Cheng, and W. Ren, Chemical vapor deposition of layered two-dimensional $MoSi_2N_4$ materials, Science **369**, 670 (2020).

[33] Z. Fei, B. Huang, P. Malinowski, W. Wang, T. Song, J. Sanchez, W. Yao, D. Xiao, X. Zhu, A. F. May, W. Wu, D. H. Cobden, J.-H. Chu, and X. Xu, Two-dimensional itinerant ferromagnetism in atomically thin Fe_3GeTe_2, Nat. Mater. **17**, 778 (2018).

[34] Y. Deng, Y. Yu, Y. Song, J. Zhang, N. Z. Wang, Z. Sun, Y. Yi, Y. Z. Wu, S. Wu, J. Zhu, J. Wang, X. H. Chen, and Y. Zhang, Gate-tunable room-temperature ferromagnetism in two-dimensional Fe_3GeTe_2, Nature (London) **563**, 94 (2018).

[35] B. Huang, G. Clark, E. Navarro-Moratalla, D. R. Klein, R. Cheng, K. L. Seyler, D. Zhong, E. Schmidgall, M. A.

McGuire, D. H. Cobden, W. Yao, D. Xiao, P. Jarillo-Herrero, and X. Xu, Layer-dependent ferromagnetism in a van der Waals crystal down to the monolayer limit, Nature (London) **546**, 270 (2017).

[36] C. Gong, L. Li, Z. Li, H. Ji, A. Stern, Y. Xia, T. Cao, W. Bao, C. Wang, Y. Wang, Z. Q. Qiu, R. J. Cava, S. G. Louie, J. Xia, and X. Zhang, Discovery of intrinsic ferromagnetism in two-dimensional van der Waals crystals, Nature (London) **546**, 265 (2017).

[37] M. Bonilla, S. Kolekar, Y. Ma, H. C. Diaz, V. Kalappattil, R. Das, T. Eggers, H. R. Gutierrez, M.-H. Phan, and M. Batzill, Strong room-temperature ferromagnetism in $\mathrm{VSe_2}$ monolayers on van der Waals substrates, Nat. Nanotechnol. **13**, 289 (2018).

[38] J. Zhou, C. Zhu, Y. Zhou, J. Dong, P. Li, Z. Zhang, Z. Wang, Y.-C. Lin, J. Shi, R. Zhang, Y. Zheng, H. Yu, B. Tang, F. Liu, L. Wang, L. Liu, G.-B. Liu, W. Hu, Y. Gao, H. Yang, W. Gao, L. Lu, Y. Wang, K. Suenaga, G. Liu, F. Ding, Y. Yao, and Z. Liu, Composition and phase engineering of metal chalcogenides and phosphorous chalcogenides, Nat. Mater. **22**, 450 (2023).

[39] J. Zhou, J. Lin, X. Huang, Y. Zhou, Y. Chen, J. Xia, H. Wang, Y. Xie, H. Yu, J. Lei, D. Wu, F. Liu, Q. Fu, Q. Zeng, C.-H. Hsu, C. Yang, L. Lu, T. Yu, Z. Shen, H. Lin, B. I. Yakobson, Q. Liu, K. Suenaga, G. Liu, and Z. Liu, A library of atomically thin metal chalcogenides, Nature (London) **556**, 355 (2018).

[40] J. Zhou, L. Shen, M. D. Costa, K. A. Persson, S. P. Ong, P. Huck, Y. Lu, X. Ma, Y. Chen, H. Tang, and Y. P. Feng, 2DMatPedia, an open computational database of two-dimensional materials from top-down and bottom-up approaches, Sci. Data **6**, 86 (2019).

[41] S. Haastrup, M. Strange, M. Pandey, T. Deilmann, P. S Schmidt, N. F Hinsche, M. N Gjerding, D. Torelli, P. M Larsen, A. C Riis-Jensen, J. Gath, K. W Jacobsen, J. J. Mortensen, T. Olsen, and K. S Thygesen, The Computational 2D Materials Database: High-throughput modeling and discovery of atomically thin crystals, 2D Mater. **5**, 042002 (2018).

[42] M. N. Gjerding, A. Taghizadeh, A. Rasmussen, S. Ali, F. Bertoldo, T. Deilmann, N. R. Knøsgaard, M. Kruse, A. H. Larsen, S. Manti, T. G. Pedersen, U. Petralanda, T. Skovhus, M. K. Svendsen, J. J. Mortensen, T. Olsen, and K. S. Thygesen, Recent progress of the computational 2D materials database (C2DB), 2D Mater. **8**, 044002 (2021).

[43] N. Mounet, M. Gibertini, P. Schwaller, D. Campi, A. Merkys, A. Marrazzo, T. Sohier, I. E. Castelli, A. Cepellotti, G. Pizzi, and N. Marzari, Two-dimensional materials from high-throughput computational exfoliation of experimentally known compounds, Nat. Nanotechnol. **13**, 246 (2018).

[44] D. Campi, N. Mounet, M. Gibertini, G. Pizzi, and N. Marzari, Expansion of the materials cloud 2D database, ACS Nano **17**, 11268 (2023).

[45] K. Choudhary, I. Kalish, R. Beams, and F. Tavazza, High-throughput identification and characterization of two-dimensional materials using density functional theory, Sci. Rep. **7**, 5179 (2017).

[46] K. Choudhary, K. F. Garrity, A. C. E. Reid, B. DeCost, A. J. Biacchi, A. R. H. Walker, Z. Trautt, J. Hattrick-Simpers, A. G. Kusne, A. Centrone, A. Davydov, J. Jiang, R. Pachter, G. Cheon, E. Reed, A. Agrawal, X. Qian, V. Sharma, H. Zhuang, S. V. Kalinin, B. G. Sumpter, G. Pilania, P. Acar, S. Mandal, K. Haule, D. Vanderbilt, K. Rabe, and F. Tavazza, The joint automated repository for various integrated simulations (JARVIS) for data-driven materials design, npj Comput. Mater. **6**, 173 (2020).

[47] A. K. Geim and I. V. Grigorieva, Van der Waals heterostructures, Nature (London) **499**, 419 (2013).

[48] R. Bistritzer and A. H. MacDonald, Moiré bands in twisted double-layer graphene, Proc. Natl. Acad. Sci. USA **108**, 12233 (2011).

[49] Y. Cao, V. Fatemi, S. Fang, K. Watanabe, T. Taniguchi, E. Kaxiras, and P. Jarillo-Herrero, Unconventional superconductivity in magic-angle graphene superlattices, Nature (London) **556**, 43 (2018).

[50] Y. Cao, V. Fatemi, A. Demir, S. Fang, S. L. Tomarken, J. Y. Luo, J. D. Sanchez-Yamagishi, K. Watanabe, T. Taniguchi, E. Kaxiras, R. C. Ashoori, and P. Jarillo-Herrero, Correlated insulator behaviour at half-filling in magic-angle graphene superlattices, Nature (London) **556**, 80 (2018).

[51] Y. Wu, D. Li, C.-L. Wu, H. Y. Hwang, and Y. Cui, Electrostatic gating and intercalation in 2D materials, Nat. Rev. Mater. **8**, 41 (2023).

[52] P. V. Nguyen, N. C. Teutsch, N. P. Wilson, J. Kahn, X. Xia, A. J. Graham, V. Kandyba, A. Giampietri, A. Barinov, G. C. Constantinescu, N. Yeung, N. D. M. Hine, X. Xu, D. H. Cobden, and N. R. Wilson, Visualizing electrostatic gating effects in two-dimensional heterostructures, Nature (London) **572**, 220 (2019).

[53] J. Ji, G. Yu, C. Xu, and H. J. Xiang, General theory for bilayer stacking ferroelectricity, Phys. Rev. Lett. **130**, 146801 (2023).

[54] X. Wan, A. M. Turner, A. Vishwanath, and S. Y. Savrasov, Topological semimetal and Fermi-arc surface states in the electronic structure of pyrochlore iridates, Phys. Rev. B **83**, 205101 (2011).

[55] G. Xu, H. Weng, Z. Wang, X. Dai, and Z. Fang, Chern semimetal and the quantized anomalous Hall effect in $\mathrm{HgCr_2Se_4}$, Phys. Rev. Lett. **107**, 186806 (2011).

[56] S. M. Young, S. Zaheer, J. C. Y. Teo, C. L. Kane, E. J. Mele, and A. M. Rappe, Dirac semimetal in three dimensions, Phys. Rev. Lett. **108**, 140405 (2012).

[57] Z. Wang, Y. Sun, X.-Q. Chen, C. Franchini, G. Xu, H. Weng, X. Dai, and Z. Fang, Dirac semimetal and topological phase transitions in $\mathrm{A_3Bi}(\mathrm{A} = \mathrm{Na, K, Rb})$, Phys. Rev. B **85**, 195320 (2012).

[58] Z. Wang, H. Weng, Q. Wu, X. Dai, and Z. Fang, Three-dimensional Dirac semimetal and quantum transport in $\mathrm{Cd_3As_2}$, Phys. Rev. B **88**, 125427 (2013).

[59] B.-J. Yang and N. Nagaosa, Classification of stable three-dimensional Dirac semimetals with nontrivial topology, Nat. Commun. **5**, 4898 (2014).

[60] Z. Wang, A. Alexandradinata, R. J. Cava, and B. A. Bernevig, Hourglass fermions, Nature (London) **532**, 189 (2016).

[61] B. Bradlyn, J. Cano, Z. Wang, M. G. Vergniory, C. Felser, R. J. Cava, and B. A. Bernevig, Beyond Dirac and Weyl fermions: Unconventional quasiparticles in conventional crystals, Science **353**, aaf5037 (2016).

[62] B. J. Wieder, Y. Kim, A. M. Rappe, and C. L. Kane, Double dirac semimetals in three dimensions, Phys. Rev. Lett. **116**, 186402 (2016).

[63] T. Zhang, Z. Song, A. Alexandradinata, H. Weng, C. Fang, L. Lu, and Z. Fang, Double-Weyl phonons in transition-metal monosilicides, Phys. Rev. Lett. **120**, 016401 (2018).

[64] P. Tang, Q. Zhou, and S.-C. Zhang, Multiple types of topological fermions in transition metal silicides, Phys. Rev. Lett. **119**, 206402 (2017).

[65] G. Chang, S.-Y. Xu, B. J. Wieder, D. S. Sanchez, S.-M. Huang, I. Belopolski, T.-R. Chang, S. Zhang, A. Bansil, H. Lin, and M. Z. Hasan, Unconventional chiral fermions and large topological Fermi arcs in RhSi, Phys. Rev. Lett. **119**, 206401 (2017).

[66] N. P. Armitage, E. J. Mele, and A. Vishwanath, Weyl and Dirac semimetals in three-dimensional solids, Rev. Mod. Phys. **90**, 015001 (2018).

[67] T. O. Wehling, A. M. Black-Schafferc, and A. V. Balatsky, Dirac materials, Adv. Phys. **63**, 1 (2014).

[68] H. C. Po, A. Vishwanath, and H. Watanabe, Symmetry-based indicators of band topology in the 230 space groups, Nat. Commun. **8**, 50 (2017).

[69] H. Watanabe, H. C. Po, and A. Vishwanath, Structure and topology of band structures in the 1651 magnetic space groups, Sci. Adv. **4**, eaat8685 (2018).

[70] B. Bradlyn, L. Elcoro, J. Cano, M. G. Vergniory, Z. Wang, C. Felser, M. I. Aroyo, and B. A. Bernevig, Topological quantum chemistry, Nature (London) **547**, 298 (2017).

[71] L. Elcoro, B. J. Wieder, Z. Song, Y. Xu, B. Bradlyn, and B. A. Bernevig, Magnetic topological quantum chemistry, Nat. Commun. **12**, 5965 (2021).

[72] J. Kruthoff, J. de Boer, J. van Wezel, C. L. Kane, and R.-J. Slager, Topological classification of crystalline insulators through band structure combinatorics, Phys. Rev. X **7**, 041069 (2017).

[73] R.-J. Slager, A. Mesaros, V. Juričić, and J. Zaanen, The space group classification of topological band-insulators, Nat. Phys. **9**, 98 (2013).

[74] M. G. Vergniory, L. Elcoro, C. Felser, N. Regnault, B. A. Bernevig, and Z. Wang, A complete catalogue of high-quality topological materials, Nature (London) **566**, 480 (2019).

[75] T. Zhang, Y. Jiang, Z. Song, H. Huang, Y. He, Z. Fang, H. Weng, and C. Fang, Catalogue of topological electronic materials, Nature (London) **566**, 475 (2019).

[76] F. Tang, H. C. Po, A. Vishwanath, and X. Wan, Comprehensive search for topological materials using symmetry indicators, Nature (London) **566**, 486 (2019).

[77] Y. Xu, L. Elcoro, Z.-D. Song, B. J. Wieder, M. G. Vergniory, N. Regnault, Y. Chen, C. Felser, and B. A. Bernevig, High-throughput calculations of magnetic topological materials, Nature (London) **586**, 702 (2020).

[78] F. Tang, H. C. Po, A. Vishwanath, and X. Wan, Efficient topological materials discovery using symmetry indicators, Nat. Phys. **15**, 470 (2019).

[79] F. Tang, H. C. Po, A. Vishwanath, and X. Wan, Topological materials discovery by large-order symmetry indicators, Sci. Adv. **5**, eaau8725 (2019).

[80] Z.-M. Yu, Z. Zhang, G.-B. Liu, W. Wu, X.-P. Li, R.-W. Zhang, S. A. Yang, and Y. Yao, Encyclopedia of emergent particles in three-dimensional crystals, Sci. Bull. **67**, 375 (2022).

[81] F. Tang and X. Wan, Exhaustive construction of effective models in 1651 magnetic space groups, Phys. Rev. B **104**, 085137 (2021).

[82] F. Tang and X. Wan, Complete classification of band nodal structures and massless excitations, Phys. Rev. B **105**, 155156 (2022).

[83] G.-B. Liu, Z. Zhang, Z.-M. Yu, S. A. Yang, and Y. Yao, Systematic investigation of emergent particles in type-III magnetic space groups, Phys. Rev. B **105**, 085117 (2022).

[84] Z. Zhang, G.-B. Liu, Z.-M. Yu, S. A. Yang, and Y. Yao, Encyclopedia of emergent particles in type-IV magnetic space groups, Phys. Rev. B **105**, 104426 (2022).

[85] N Lazić, V Damljanović, and M Damnjanović, Fully linear band crossings at high symmetry points in layers: Classification and role of spin–orbit coupling and time reversal, J. Phys. A: Math. Theor. **55**, 325202 (2022).

[86] Z. Zhang, W. Wu, G.-B. Liu, Z.-M. Yu, S. A. Yang, and Y. Yao, Encyclopedia of emergent particles in 528 magnetic layer groups and 394 magnetic rod groups, Phys. Rev. B **107**, 075405 (2023).

[87] X. Zhang, F. Zangeneh-Nejad, Z.-G. Chen, M.-H. Lu, and J. Christensen, A second wave of topological phenomena in photonics and acoustics, Nature (London) **618**, 687 (2023).

[88] W. Zhu, W. Deng, Y. Liu, J. Lu, H.-X. Wang, Z.-K. Lin, X. Huang, J.-H. Jiang, and Z. Liu, Topological phononic metamaterials, Rep. Prog. Phys. **86**, 106501 (2023).

[89] T. Ozawa, H. M. Price, A. Amo, N. Goldman, M. Hafezi, L. Lu, M. C. Rechtsman, D. Schuster, J. Simon, O. Zilberberg, and I. Carusotto, Topological photonics, Rev. Mod. Phys. **91**, 015006 (2019).

[90] P. A. McClarty, Topological Magnons: A review, Annu. Rev. Condens. Matter Phys. **13**, 171 (2022).

[91] See Supplemental Material I at http://link.aps.org/supplemental/10.1103/PhysRevB.109.205141 for all positions of all LBCs in the 80 LGs for the four settings NTRS,NSOC, NTRS,SOC, TRS,NSOC and TRS,SOC; all explicit representation matrices for the little groups of all LBCs and all symmetry-related LBCs.

[92] See Supplemental Material II at http://link.aps.org/supplemental/10.1103/PhysRevB.109.205141 for the 1707 2D materials hosting coexisting LBCs in both electronic and phononic band structures, the 3035 2D materials necessarily and only necessarily hosting electronic LBCs, the coexisting LBCs in both electronic and phononic band structures of the 66 2D materials which we calculated, and the detailed computational methods, which includes Refs. [40,97].

[93] C. Bradley and A. Cracknell, *The Mathematical Theory of Symmetry in Solids: Representation Theory for Point Groups and Space Groups* (Oxford University Press, Oxford, 2009).

[94] https://cryst.ehu.es/cgi-bin/subperiodic/programs/nph-sub_wp.

[95] W. Meng, Y. Liu, W. Yu, X. Zhang, and G. Liu, Spin-orbital robust Dirac points in two-dimensional systems, Mater. Today Phys. **27**, 100774 (2022).

[96] J. Gong, J. Wang, H. Yuan, Z. Zhang, W. Wang, and X. Wang, Dirac phonons in two-dimensional materials, Phys. Rev. B **106**, 214317 (2022).

[97] V. Wang, N. Xu, J.-C. Liu, G. Tang, and W.-T. Geng, VASPKIT: A user-friendly interface facilitating high-throughput computing and analysis using VASP code, Comput. Phys. Commun. **267**, 108033 (2021).

[98] D. Wang, F. Tang, J. Ji, W. Zhang, A. Vishwanath, H. C. Po, and X. Wan, Two-dimensional topological materials discovery by symmetry-indicator method, Phys. Rev. B **100**, 195108 (2019).

[99] G. Kresse and J. Furthmüller, Efficient iterative schemes for ab initio total-energy calculations using a plane-wave basis set, Phys. Rev. B **54**, 11169 (1996).

[100] G. Kresse and J. Furthmüller, Efficiency of ab-initio total energy calculations for metals and semiconductors using a plane-wave basis set, Comput. Mater. Sci. **6**, 15 (1996).

[101] G. Kresse and D. Joubert, From ultrasoft pseudopotentials to the projector augmented-wave method, Phys. Rev. B **59**, 1758 (1999).

[102] J. P. Perdew, K. Burke, and M. Ernzerhof, Generalized gradient approximation made simple, Phys. Rev. Lett. **77**, 3865 (1996).

[103] J. P. Perdew, A. Ruzsinszky, G. I. Csonka, O. A. Vydrov, G. E. Scuseria, L. A. Constantin, X. Zhou, and K. Burke, Restoring the density-gradient expansion for exchange in solids and surfaces, Phys. Rev. Lett. **100**, 136406 (2008).

[104] A. Togo and I. Tanaka, First principles phonon calculations in materials science, Scr. Mater. **108**, 1 (2015).

[105] J. Gao, Q. Wu, C. Persson, and Z. Wang, Irvsp: To obtain irreducible representations of electronic states in the VASP, Comput. Phys. Commun. **261**, 107760 (2021).